SUPPORTING INFORMATION

Effect of Oxidation on the Mechanochemical synthesis of bismuth telluride nanophases, ex-situ and in-situ structural characterization and thermoelectric properties

Marcelo Augusto Malagutti[a], Rayner Enriquez Camps[b], Umberto Anselmi-Tamburini[c], Robert E. Dinnebier[d], Claudia Weidenthaler[e], Paolo Scardi[a], Carlos Eduardo Maduro de Campos[b]*

[a] *Department of Civil, Environmental and Mechanical Engineering, University of Trento, via Mesiano 77, 38123 Trento, Italy.*

[b]*Laboratório de Síntese e Caracterização de nanoMateriais - Departamento de Física, Universidade Federal de Santa Catarina, 88040-900 Florianópolis – SC, Brazil.*

[c]*Department of Chemistry, University of Pavia, 27100 Pavia, Italy.*

[d]*Max Planck Institute for Solid State Research, Heisenbergstrasse 1, 170569, Stuttgart, Germany*.

[e]*Max-Planck-Institut fur Kohlenforschung, Heterogeneous Catalysis, Kaiser-Wilhelm-Platz 1, 45470 Mülheim an der Ruhr, Germany.*

**Corresponding author email: carlos.campos@ufsc.br*

Supplementary Note 1: Reagents oxidation

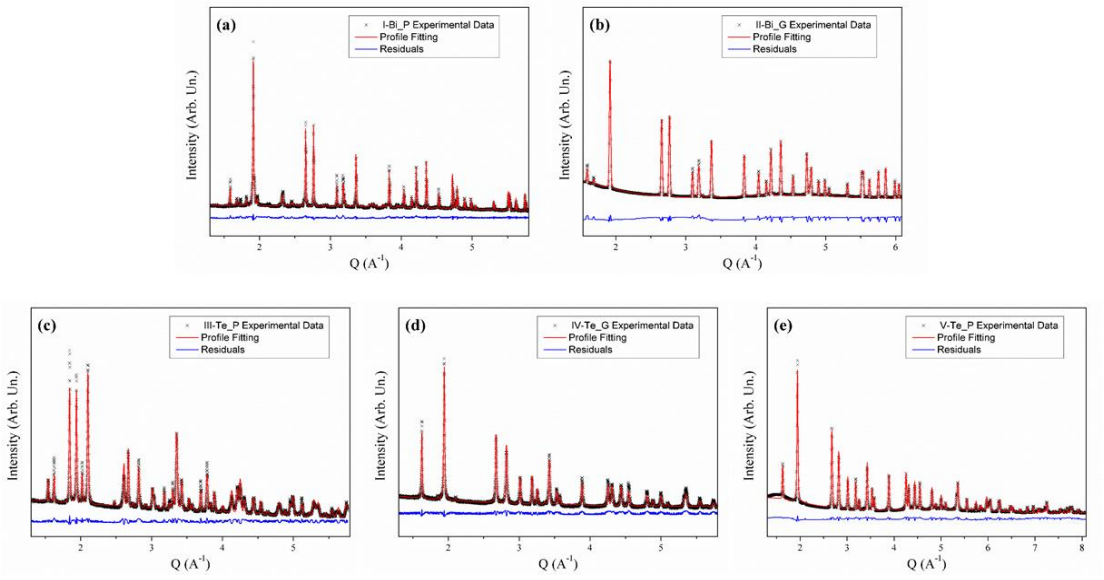

Figure S 1. All data collection and refinements described in Supplementary Note 2. (a) Bi powder, (b) Bi granules, (c) Te powder, (d) Te granules, and (e) Te powder. Oxidation is observed in Bi powder (a), Te powder (c), and Te granules (d), while no oxidation was detected in Bi granules (b) and Te powder (e). The Circular markers represent experimental data, the red lines the profile fit, and the blue lines the residuals.

Supplementary Note 2: sample phase determination

The kinetics of the reaction of the samples 1-Bi50Te-BM1a, 2-Bi50Te-BM1b, 5-Bi70Te-BM1 were measured in a Xpert MPD equipped with a X´celerator detector using Cu (Kα 1.5418 Å) radiation in a Bragg-Brentano geometry and Si zero-background sample holders. The final milling time of these powders were measured at ambient conditions in the ID31 beam line of ESRF using a brand new-designed sample holder ruler. PXRD and PDF data were recorded at the beamline using a DECTRIS Pilatus3 X 2 M CdTe area detector. The wavelength and geometry of the instrument were refined using a LaB6 standard (NISTSRM660c) using the program PyFAI [31]. The photon energy used was 75 keV and the sample to detector distance was 1500 mm for XRD and 300 mm for PDF. The raw area detector data were azimuthally integrated to intensity vs. 2θ using the MatFRAIA algorithm [32]. These samples were also evaluated by in-situ XRD experiments under temperature variations (up to 500- 600°C) using a blower furnace in a Stoe Stadi-P equipped with a Mythen Dectris detector using Ag (Kα1 Ge(111) 0.55941 Å) radiation in Debye Scherrer geometry. The samples were packed in 0.3 mm diameter quartz capillaries. Samples recovered from DTA measurements were analyzed in an Empyrean diffractometer using Cu (Kα 1.5418 Å and Kα1 Hibrid Grafite Monochromator 1.5406 Å) radiation in Bragg-Brentano geometry using Si zero-background sample holders and at the DanMAX beamline at the MAX-IV Laboratory.

The real-time in-situ XRD experiments were performed in the P02.1 beamline at DESY [33,34] using 60 keV photon energy. The final milled samples were packed in 0.8 mm diameter boroscilicate glass capillaries. PXRD and PDF data were recorded at the beamline using a λ of 0.20741 Å (~60 keV) and a 2D area detector (XRD 1621 from PerkinElmer [35]). The sample to detector distance was 2100 mm for XRD and 300 mm for PDF.

The samples recovered from thermoelectric characterization were analyzed in a Bruker D8 Discover using Co (Kα 1.78897 Å) radiation in a Bragg-Brentano geometry. The sample disks were attached to the sample holder and measured within an angular range of 12-94° in 2θ.

The high purity reactants used for the real-time mechanochemical experiments (Bi_G and Te_P2) were also measured at the DanMAX beamline. The samples were packed in 0.3 mm diameter boroscilicate glass capillaries. PXRD data was recorded at the DanMAX beamline using a DECTRIS Pilatus3 X 2 M CdTe area detector. The wavelength and geometry of the instrument were refined using a LaB6 standard (NISTSRM660c) using the program PyFAI [31]. The photon energy used was 31.50 keV and the sample to detector distance was 400 mm. The raw area detector data were azimuthally integrated to intensity vs. 2θ using the MatFRAIA algorithm [32].

Table S 1. List of XRD measurements performed for all the samples.

ID	Sample	Xpert MPD	Stoe	Empyrean	D8	ESRF-ID31	Dan-MAX-IV	Desy
1	Bi50Te-BM1a	X	HT X	DTA X	X-TE	X - PDF XRD	DTA X	
2	Bi50Te-BM1b	X	HT X	DTA X	X-TE	X -PDF XRD	DTA X	
3	Bi50Te-BM2a							X - PDF
4	Bi70Te-BM1	X	HT X	DTA X	X-TE	X -PDF	DTA X	
5	Bi70Te-BM2a							X - PDF
5	Bi70Te-BM2a-SPS				X			
II	Bi_G						X	
IV	Te_G						X	
V	Te_P2						X	

HT stands for high temperature measurements. DTA means that the samples were measured after DTA experiments. PDF means that PDF data was collected. TE means collected after thermoelectric characterization.

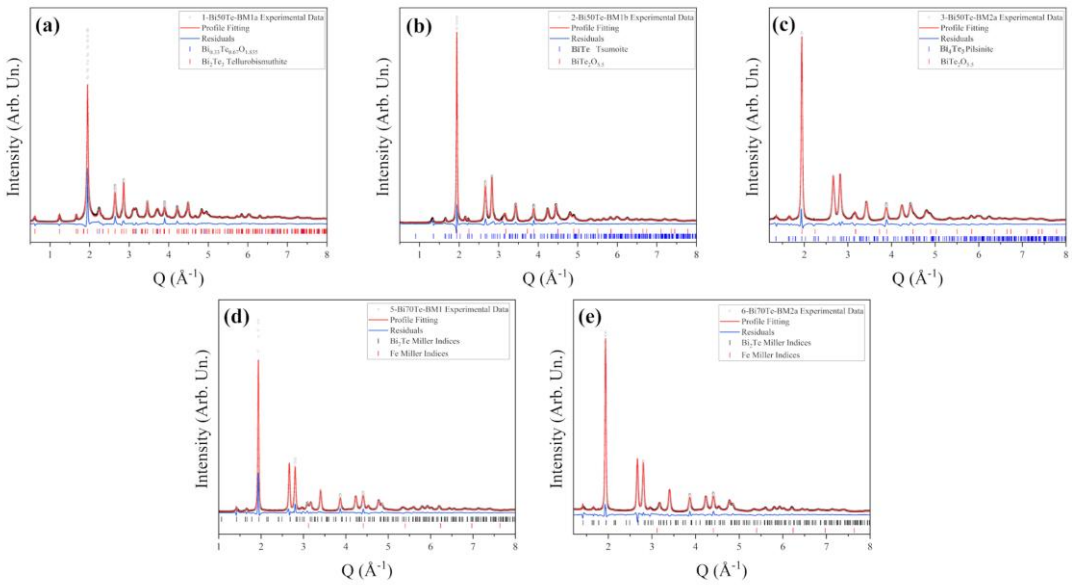

Figure S 2. Rietveld refinements performed on the diffraction data collected from the as-milled powders. (a) $Bi_{50}Te$–BM1a with phases identified as Bi_2Te_3 and $Bi_{0.33}Te_{0.67}O_{1.835}$; (b) $Bi_{50}Te$–BM1b consisting of BiTe and $BiTe_2O_{5.5}$; (c) $Bi_{50}Te$–BM2a consisting of Bi_4Te_3 and $BiTe_2O_{5.5}$; (d) $Bi_{70}Te$–BM1 composed of Bi_2Te with Fe contamination; and (e) $Bi_{70}Te$–BM2a composed of Bi_2Te with Fe contamination. Circular markers represent experimental data, red lines the profile fitting, and blue lines the residuals; vertical ticks indicate Bragg reflection positions of the identified phases.

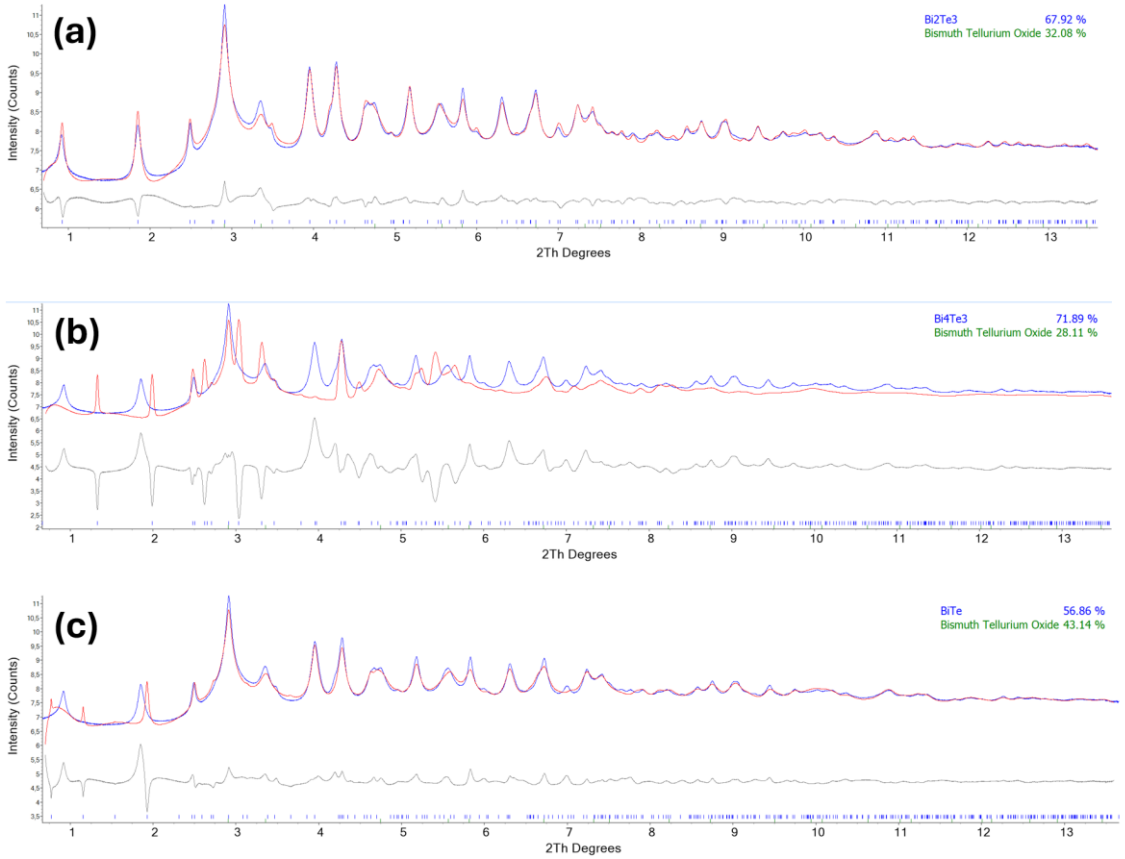

Figure S 3. 1-Bi50Te-BM1a modelled with: (a) Bi2Te3 and (b) Bi4Te3, and (c) BiTe phases

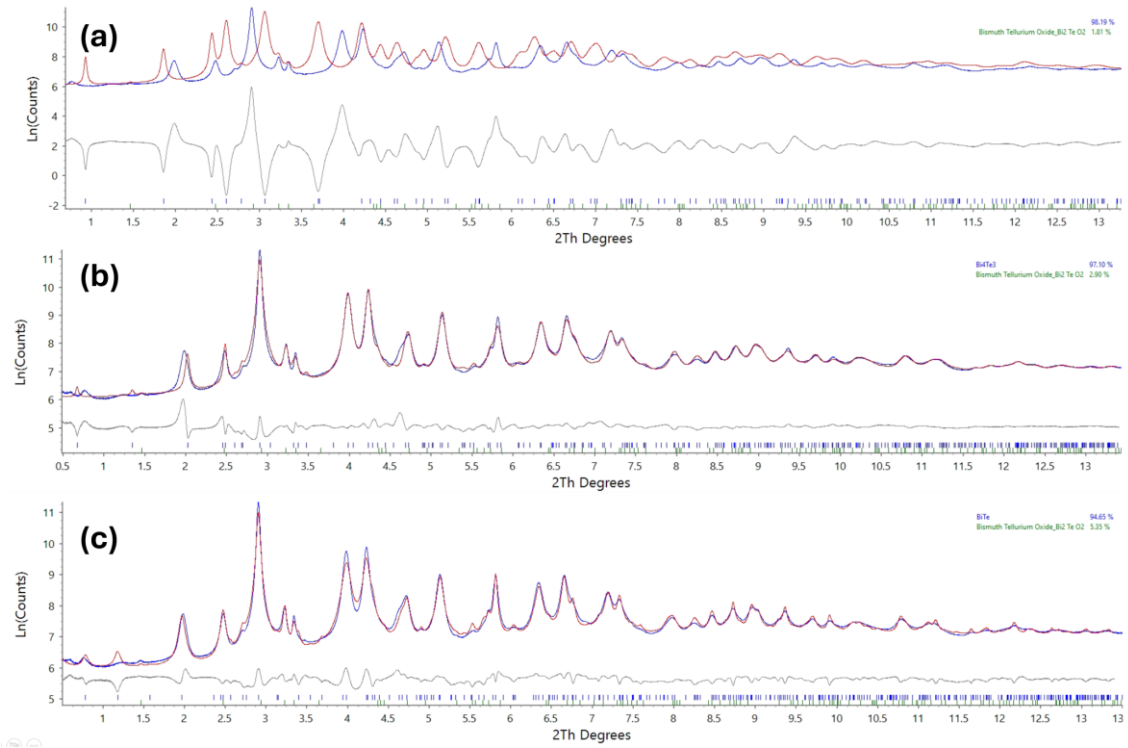

Figure S 4. 2-Bi50Te-BM1b modelled with: (a) Bi2Te3 and (b) Bi4Te3, and (c) BiTe phases.

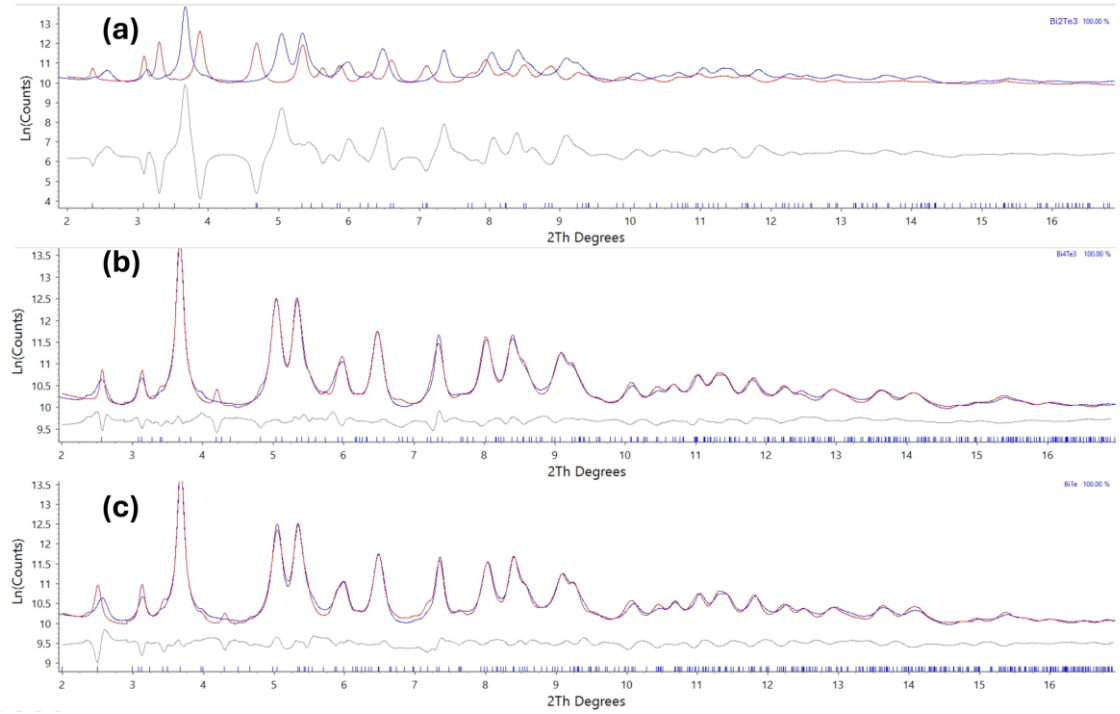

Figure S 5. 3-Bi50Te-BM2a modelled with: (a) Bi2Te3 and (b) Bi4Te3, and (c) BiTe phases.

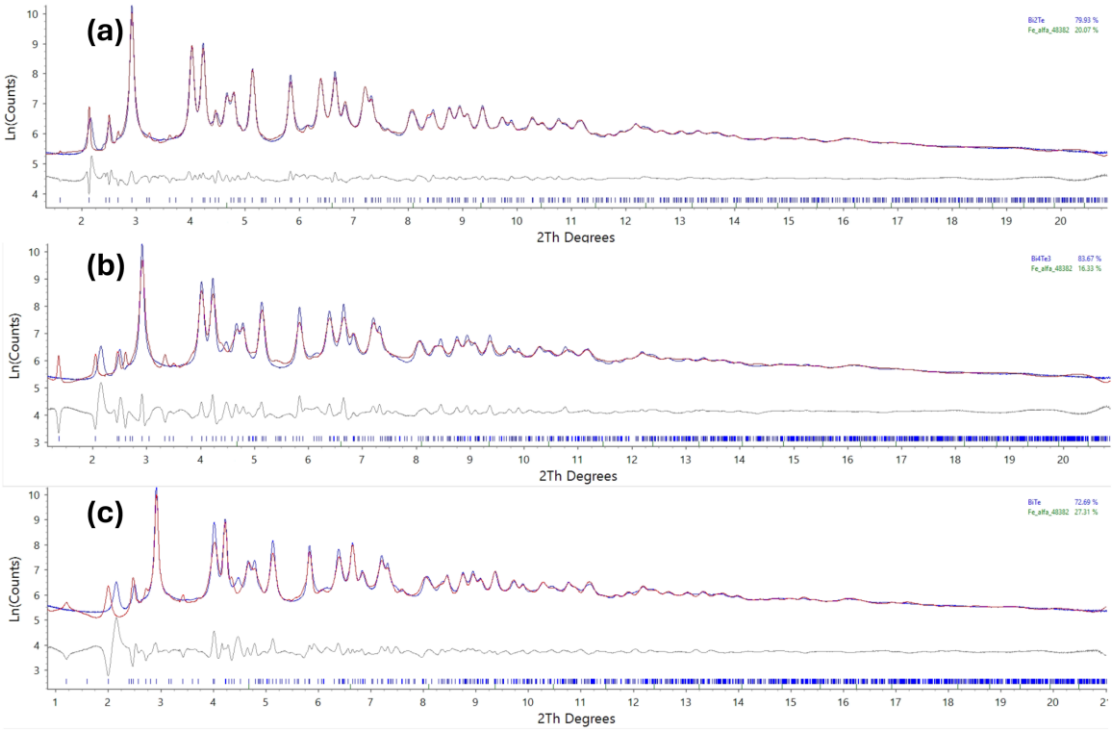

Figure S 6. 5-Bi70Te-BM1 modelled with: (a) Bi2Te and (b) Bi4Te3, and (c) BiTe phases.

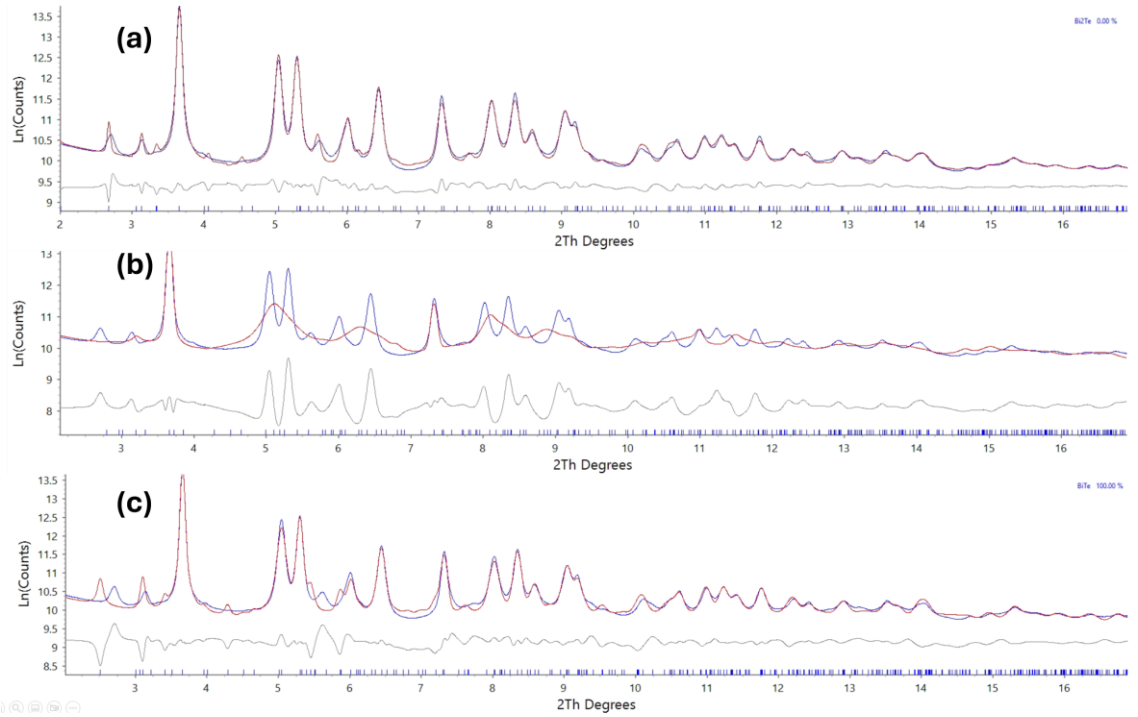

Figure S 7. 6-Bi70Te-BM2a modelled with: (a) Bi2Te and (b) Bi4Te3, and (c) BiTe phases.

Table S 2. C_p estimated using the Neumann-Kopp law and density estimated using the geometric method. Uncertainties were estimated given the caliper and weight scale uncertainties of $5 \times 10^{-5} g$ and 5×10^{-4} cm, respectively.

Sample	Cp (J K^{-1} g^{-1})	Density (g cm^{-3})	Theoretical Density (g cm^{-3})	Theoretical Density (%)	Porosity Φ (%)
1-Bi50Te-BM1a	0.148208	6.20(4)	7.85	79.0(5)	21.0(5)
2-Bi50Te-BM1b	0.148208	6.66(4)	8.225	81.0(5)	19.0(5)
3-Bi50Te-BM2a	0.148208	6.9(1)	8.448	82(1)	18(1)
5-Bi70Te-BM1	0.135138	7.04(4)	8.776	80.2(4)	19.8(4)
6-Bi70Te-BM2a	0.135138	7.05(3)	8.776	80.3(4)	19.7(4)
5-Bi70Te-BM2a-SPS	0.135138	8.37(6)	8.776	95.4(7)	4.6(7)

Table S 3. XRPD parameters results. Phase percentage, lattice parameters a and c, volume of the unit cell V, crystallite size L, and microstrain parameter s.

Sample	Phase	%	*a* (Å)	*c* (Å)	V (Å³)	L	S	Rwp	Instrument
1-Bi50Te-BM1a	Bi_2Te_3	88.76	4.3917(6)	30.467(6)	508.89	18.8(4)	1.41(3)	7.29	Xpert MPD
		70.0(5)	4.3901(1)	30.453(2)	508.28(5)	33	1.168(11)	11.40	ESRF
2-Bi50Te-BM1b	BiTe	98.0(2)	4.4474(6)	23.854(4)	408.59(12)	45.5(18)	1.706(16)	8.23	Xpert MPD
		97.05(13)	4.44279(17)	23.8575(17)	407.82(4)	34.3(5)	1.516(9)	14.44	ESRF
3-Bi50Te-BM2a	Bi_4Te_3	100	4.4339(3)	41.492(4)	706.44(11)	33.1(8)	1.951(14)	11.59	DESY
			4.4297(3)	41.539(5)	705.90(12)	35.2(10)	1.991(16)	11.59	
5-Bi70Te-BM1	Bi_2Te	86.3(7)	4.4872(4)	17.806(2)	310.49(7)	57.0(18)	1.146(12)	6.66	Xpert MPD
		88.0(4)	4.48405(13)	17.8049(9)	310.04(2)	51.6(9)	1.131(6)	16.29	ESRF
6-Bi70Te-BM2a	Bi_2Te	100	4.48819(16)	17.7859(11)	310.28(3)	46.3(8)	1.585(8)	10.82	DESY

2.1 Raman analysis

The Raman spectra of the Bi–Te samples, together with their corresponding multipeak fits performed using Lorentzian line shapes, are shown in Figure S 8(a). Figure S 8(b) presents the magnified 80–220 cm^{-1} region, where the deconvolution highlights the spectral response dominated by Bi–Te vibrational modes. Across all samples, the characteristic Raman features of the Bi–Te system are identified, with peaks at approximately 98–102 and 131–134 cm^{-1} corresponding to the E_g^2 and A_{1g}^2 modes of Bi_2Te_3, respectively. These values are consistent with those reported in the literature [1] and serve as a reference framework for evaluating how the vibrational structure evolves with mechanical processing and variations in the Bi/Te ratio.

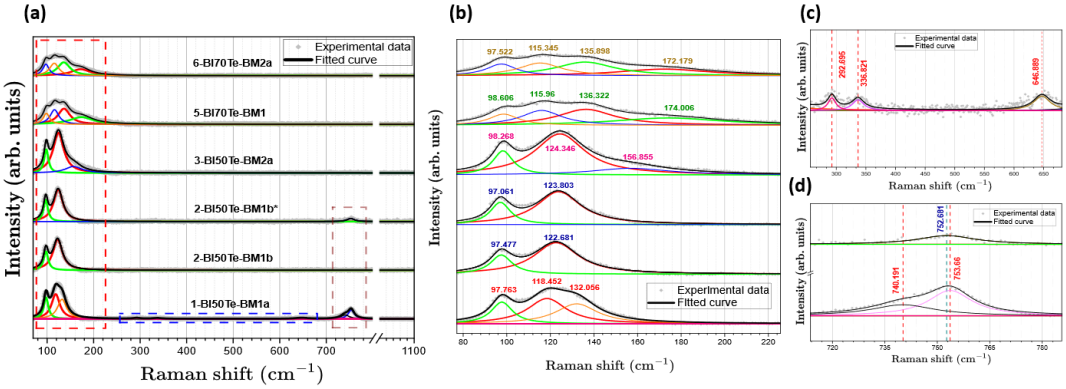

Figure S 8. Raman spectra and multipeak fitting of the Bi–Te samples. (a) Full Raman spectra with corresponding fitted curves for all samples. The asterisk (*) indicates a spectrum acquired from an additional region of the same sample. (b–d) Magnified views of the regions highlighted in red, blue, and brown, respectively, showing the deconvoluted vibrational modes and their corresponding fitted peak positions.

In sample 1-Bi50Te-BM1a, these modes are clearly observed, accompanied by bands at 292.7, 336.8, and within the 647–754 cm^{-1} range. These additional features are attributable to oxidized phases, primarily α-Bi_2O_3 [2], δ-Bi_2O_3 [3], and Bi–Te–O ternary compounds [4], [5]. Although these signals appear with lower relative intensities, they indicate the presence of oxide species, in agreement with the XRD analysis. Similarly, in 2-Bi50Te-BM1b*, a vibrational feature at 756

cm^{-1} was detected [Figure S 8(c) and (d)], which is characteristic of Bi–Te–O ternary systems. The presence of an oxygen-rich phase is particularly relevant, as it explains why certain oxide bands appear more intense than expected for purely superficial oxidation: in these samples, oxide formation is not restricted to the surface but corresponds to a crystalline phase detected by XRD, reinforcing the Raman assignment. This scenario indicates that mechanical milling not only introduces disorder but also promotes oxygen incorporation and the stabilization of oxidized compounds.

Table S 4. Raman shifts (cm⁻¹) for the different phases identified in the Bi–Te system, including Bi_2Te_3, BiTe, and Bi_4Te_3. Values reported as "a" correspond to measurements obtained in this work. Literature references are listed in the rightmost column. The asterisk (*) denotes spectra acquired from an additional region of the same sample.

Sample / phase	Raman shift (cm−1)										Ref.
1-Bi50Te-BM1a	97.763	118.452	132.056			292.695	336.821	646.889	740.191	753.66	a
Bi_2Te_3	102.3		134								[6]
	99.3		131								[7]
	101.1		132.7								[1]
	101.2		132.9								[8]
	102.3		134								[9]
	99	120	141								[10]
	98	121	140								[10]
	101.4	116.5	132.9								[11]
2-Bi50Te-BM1b	97.477	122.681									a
2-Bi50Te-BM1b*	97.061	123.803								752.681	a
BiTe	100	117									[6]
	100.1	119.6									[7]
	102	120	127								[12]
	101.8	117.1									[8]
3-Bi50Te-BM2a	98.268	124.346		156.855							a
Bi_4Te_3	98										[6]
	99.8	109.8									[7]
	100	114.9	132.2								[1]
	100.1	109.5									[8]
5-Bi70Te-BM1	98.606	115.96	136.322		174.006						a
6-Bi70Te-BM2a	97.522	115.345	135.898		172.179						a

Direct comparison with sample 2-Bi50Te-BM1b reveals additional structural distinctions despite both materials sharing the same nominal Bi–Te stoichiometry. In BM1b, the Raman spectrum exhibits a pronounced suppression of the A_{1g}^2 mode (~133 cm^{-1}) accompanied by the emergence of a well-defined band at ~122–124 cm^{-1}, a frequency range in which no Raman-active mode is expected for Bi_2Te_3. Crucially, the appearance or suppression of modes in this region cannot be attributed to stacking disorder, turbostratic effects, or intergrowth defects within a Bi_2Te_3-type structure, as such perturbations typically lead only to peak broadening or modest frequency shifts and do not generate additional Raman-active modes nor eliminate symmetry-allowed ones.

Instead, the band at ~122–124 cm^{-1} corresponds to the characteristic vibrational response of BiTe, whose layered architecture, comprising Bi bilayers inserted between Bi_2Te_3 blocks, modifies the local coordination environment and relaxes the symmetry selection rules that govern the Raman modes of the R-3m Bi_2Te_3 framework. This altered bonding environment can activate additional Raman modes while simultaneously suppressing Bi_2Te_3-derived vibrations,

including the high-frequency A_{1g}^2 mode, thus providing a consistent explanation for the spectral differences observed between BM1a and BM1b.

Sample 3-Bi50Te-BM2a exhibits an even more modified vibrational pattern. Although the mode at ~98 cm^{-1} persists, the other peaks shift to 124.346 and 156.855 cm^{-1}. Raman spectroscopy therefore confirms a structural transition toward a Bi-richer environment, consistent with Bi_4Te_3, where the incorporation of bismuthene-like units produces a more pronounced peak shift [13]. The emergent mode near 157 cm^{-1} is particularly significant: it does not correspond to any of the vibrational modes of the conventional binary phases of the Bi–Te system and must be interpreted as arising from internal distortions induced by Bi enrichment or from local rearrangements of the lattice.

The Bi-rich samples (5-Bi70Te-BM1 and 6-Bi70Te-BM2a) further support this trend. Both exhibit new modes at 172–174 cm^{-1}, a vibrational signature absents from the classic Bi_2Te_3, BiTe, or Bi_4Te_3 phases and therefore attributable to a chemically modified environment enriched in bismuth, consistent with Bi_2Te. The persistence of these modes in both BM1 and BM2a, regardless of minor differences in milling conditions, suggests that their origin is directly linked to Bi enrichment rather than to mechanical processing alone. The fact that these modes replace or shift the original features near 120 and 140 cm^{-1} observed in the less Bi-rich samples indicates a structural transition in which the lattice loses the vibrational characteristics of Bi_2Te_3 and adopts the behavior of a stiffer—i.e., higher force-constant—and possibly more disordered phase.

Overall, the analysis reveals that the Bi–Te system responds sensitively to compositional changes, particularly Bi enrichment. A critical comparison demonstrates that the vibrational evolution is not linear but follows a well-defined sequence: Bi_2Te_3 → BiTe → Bi_4Te_3 → Bi_2Te, accompanied by the emergence of new modes acting as markers of local lattice restructuring. This correlation between crystalline structure and vibrational response confirms that compositional modification governs both the rigidity of the chemical bonds and the chemical stability of the system.

2.2. Milling time evolution

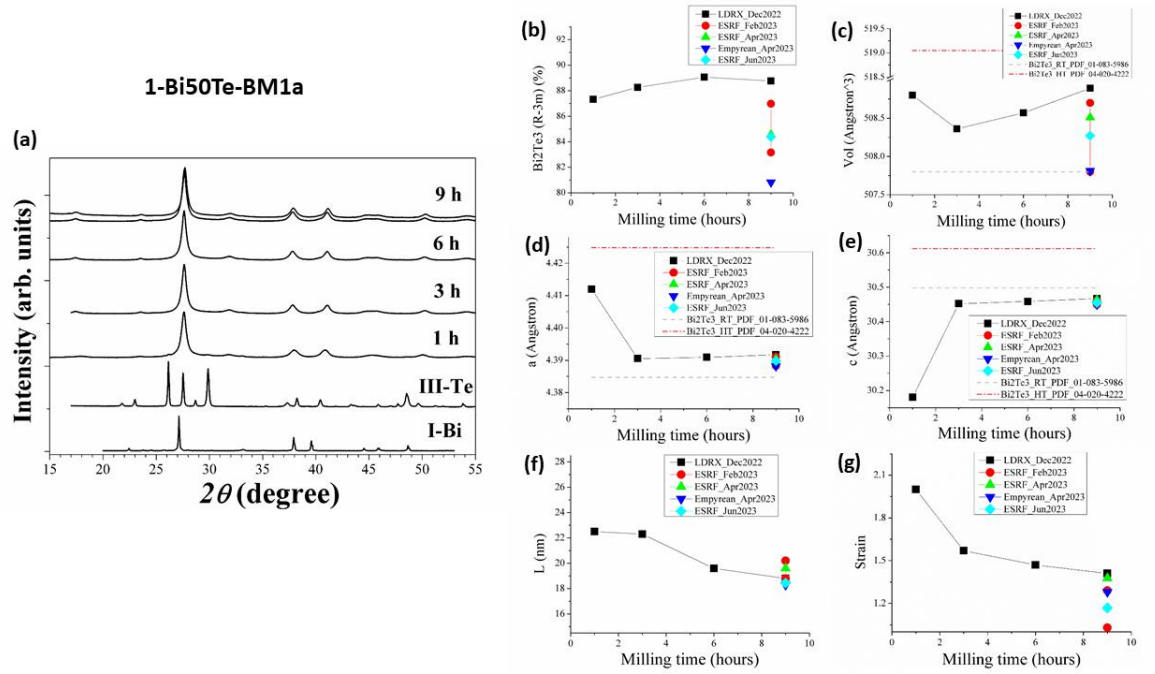

Figure S 9. Structural evolution of 1-Bi50Te-BM1a sample during mechanochemical synthesis as a function of milling time. (a) X-ray diffraction patterns showing the progressive formation of Bi_2Te_3 after 1–9 h of milling. Evolution of structural parameters obtained from Rietveld refinements: (b) phase fraction of Bi_2Te_3, (c) unit-cell volume, (d) lattice parameter a, (e) lattice parameter c, (f) crystallite size (L), and (g) microstrain. The different colors in panels (b–g) correspond to measurements carried out at different times in order to evaluate the stability of the sample. Reference values for Bi_2Te_3 at room temperature (RT) and high temperature (HT) are shown as dashed lines.

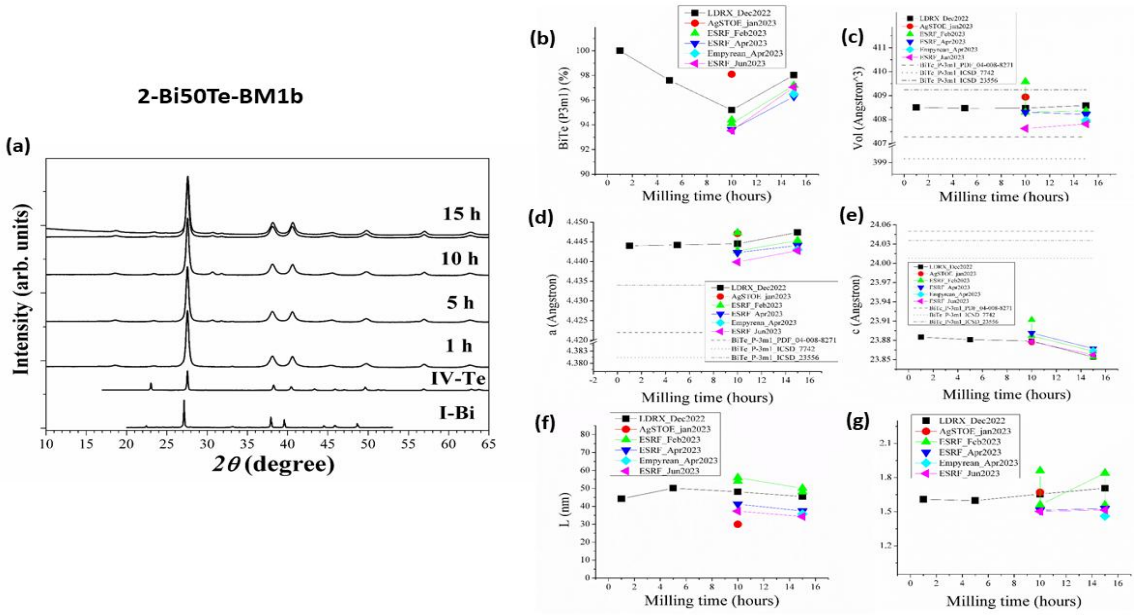

Figure S 10. Structural evolution 2-Bi50Te-BM1b sample during mechanochemical synthesis as a function of milling time. (a) X-ray diffraction patterns showing the transformation of the initial elements to BiTe phases after 1–15 h of milling. Evolution of the structural parameters obtained from Rietveld refinements: (b) BiTe phase fraction, (c) unit cell volume, (d) lattice parameter a, (e) lattice parameter c, (f) crystallite size (L), and (g) microstrain. The different colors in panels (b–g) correspond to measurements performed at different times to assess the sample stability. The reported reference values for BiTe are shown as dashed lines.

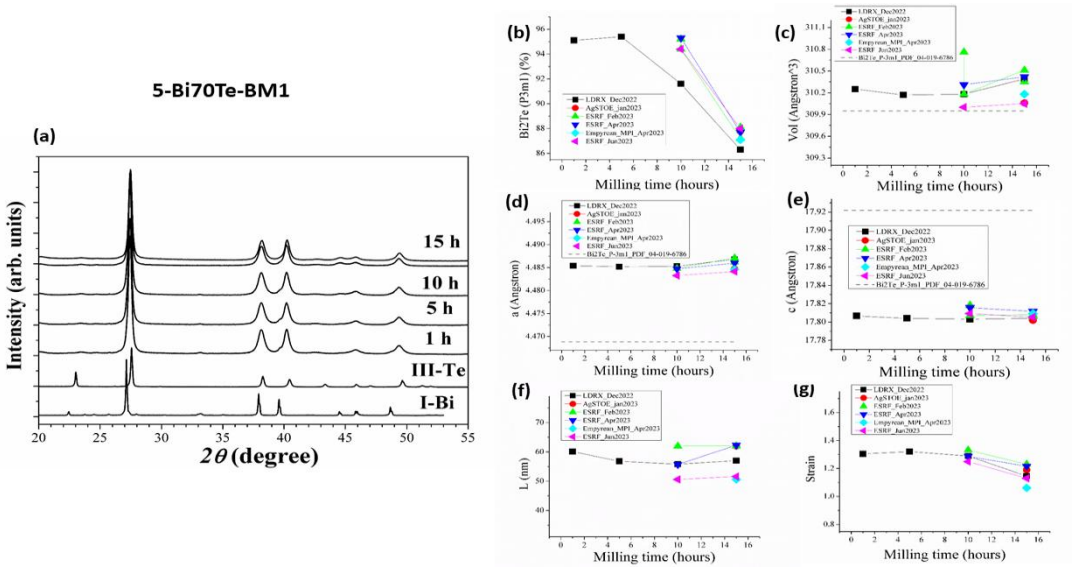

Figure S 11. Structural evolution of the 5-Bi70Te-BM1 sample during mechanochemical synthesis as a function of milling time. (a) X-ray diffraction patterns showing the transformation of the initial elements into the Bi2Te phase after 1–15 h of milling. Evolution of the structural parameters obtained by Rietveld refinements: (b) Bi2Te phase fraction, (c) unit cell volume, (d) lattice parameter a, (e) lattice parameter c, (f) crystallite size (L), and (g) microstrain. The different colors in panels (b–g) correspond to measurements performed at different times to assess the sample stability. The reported reference value for Bi2Te is shown as dashed lines.

2.3 TEM particle size analysis

The particle size histograms exhibit broad distributions that follow a log-normal function. Although Figure 6 presents the data on a linear scale, complementary statistical analyses (Q–Q plots provided in Figure S12) confirm the log-normal behavior.

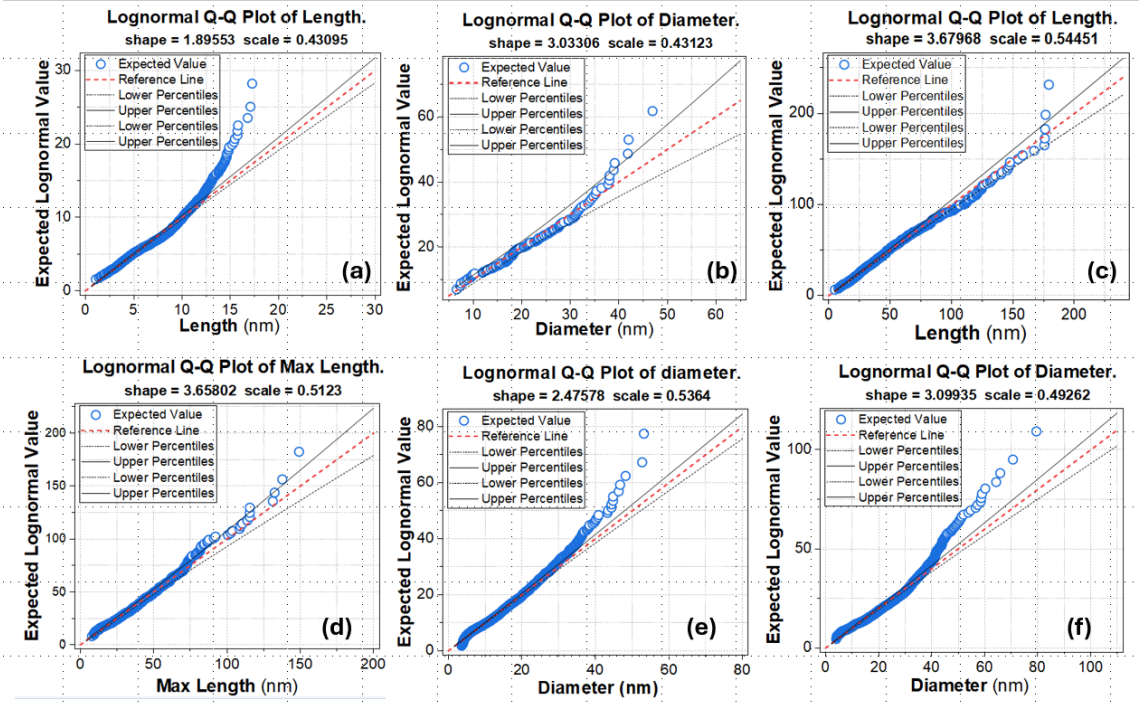

Figure S 12. Lognormal Q–Q plots of particle length for samples (a) 1-Bi50Te-BM1a, (b) 2-Bi50Te-BM1b, (c) 5-Bi70Te-BM1, (d) BM1a-tt, (e) BM1b-tt, and (f) BM1-tt. The red line represents the theoretical lognormal distribution.

The lognormal Q–Q plots in Figure S12 evaluate the agreement between the experimental particle size distributions and the theoretical lognormal model. The close alignment of the empirical quantities with the reference line across all panels confirms that the logarithm of the particle size follows an approximately normal distribution, thereby supporting a lognormal behavior in the original (non-transformed) data domain.

In these fits, the reported shape and scale parameters correspond to the lognormal location (μ) and dispersion (σ), respectively. The estimated μ values (≈1.9–3.7) and σ values (≈0.43–0.54) indicate moderate variability in logarithmic space. Samples with larger μ values (e.g., panels (c)–(d)) exhibit broader particle size ranges and higher upper percentiles, whereas those with smaller μ (panels (a)–(b)) display narrower distributions concentrated below approximately 30 nm.

Slight deviations from linearity at the upper quantiles remain within one logarithmic standard deviation and are not statistically significant. Overall, the obtained μ and σ parameters accurately characterize both the central tendency and dispersion of the logarithmically transformed data, confirming that the lognormal model provides a consistent and quantitatively reliable representation of particle size variability across all analyzed samples.

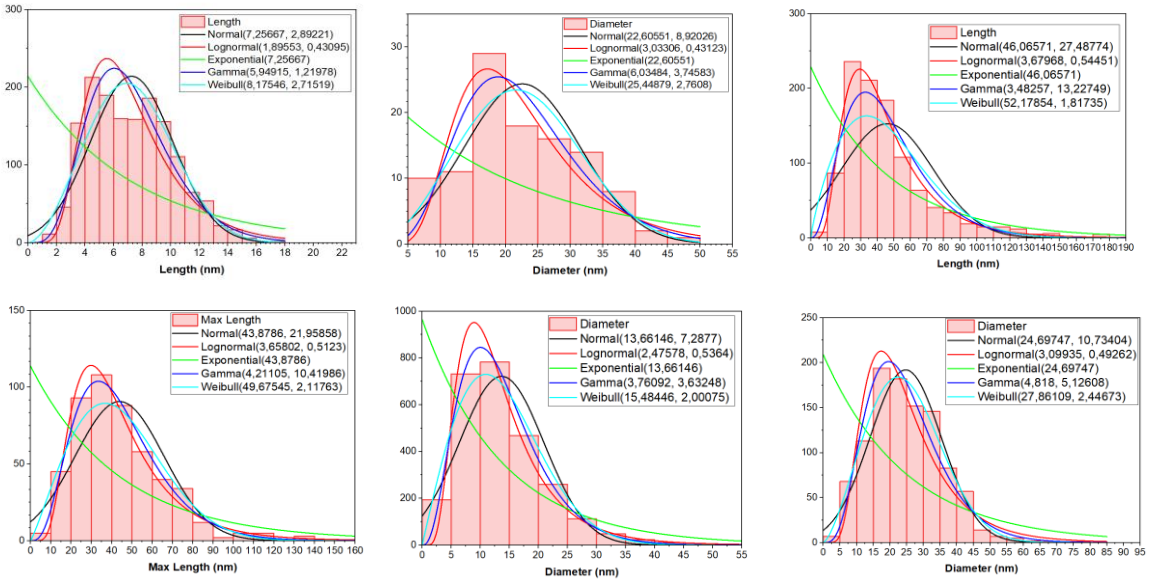

Figure S 13. Figure S13. Particle size distributions fitted to different statistical models for samples (a) 1-Bi50Te-BM1a, (b) 2-Bi50Te-BM1b, (c) 5-Bi70Te-BM1, (d) BM1a-tt, (e) BM1b-tt, and (f) BM1-tt. The histograms represent the experimental data, while the curves correspond to the best fits obtained using Normal, Lognormal, Exponential, Gamma, and Weibull functions.

Particle size histograms obtained from TEM measurements were fitted to several statistical models, including Normal, Lognormal, Exponential, Gamma, and Weibull distributions (Figure S13). Among these, the Lognormal function provides the best agreement with the experimental data for all samples. This result indicates that the evolution of particle size during mechanical milling is governed by stochastic and multiplicative processes, rather than purely additive or random processes.

In mechanical alloying, repeated fracture, cold welding, and plastic deformation of particles occur in a highly dynamic and non-uniform manner. Each event modifies the size of individual particles in proportion to their current size, leading to a cumulative multiplicative effect. As a consequence, the logarithm of the particle size tends to follow a normal distribution, while the particle size itself follows a lognormal distribution. This statistical behavior is characteristic of systems governed by growth or fragmentation processes with proportional effects and has been widely documented in the literature of mechanochemistry and powder metallurgy.

Therefore, the predominance of lognormal distributions in the present study corroborates the interpretation that the evolution of particle size during ball milling is mainly controlled by random fracture-weld cycles and heterogeneities in energy transfer inherent to the milling process. The other models tested (Normal, Gamma, Weibull, and Exponential) failed to reproduce the strong right tail observed in the experimental histograms, confirming that the lognormal distribution more accurately represents the physical mechanisms underlying particle size formation in these systems.

2.4 Selected Area Electron Diffraction phase identification

Table S 5. Interplanar spacings (d, nm) for the different phases identified in the Bi–Te system. Values marked with "a" correspond to the spacings measured from the HRTEM images acquired in this work, while the remaining entries represent d-spacings reported from HRTEM analyses in the literature.

Sample/ phase		**Interplanar spacings (d, nm)**				**Ref.**	**Coment**
1-Bi50Te-BM1a	0.321 nm (015)	0.327 nm* (015)				a	*tt
Bi_2Te_3	0.2195 nm (110)					[14]	Bi_2Te_3 was synthesized by solvothermally reacting the $BiCl_4^-$–CTA^+ lamellar precursor with Te powder and reducing the mixture with $NaBH_4$ Bi2Te3 nanoplates prepared at 210 °C with the solvent volume ratio of 1:6
	0.323 nm (015)					[15]	Bi_2Te_3 nanowires were synthesized by first producing Te nanowires via hydrazine reduction of TeO_2 in TOPO/ethylene glycol, followed by a hydrothermal reaction of the Te nanowires with $BiCl_3$ and NaOH at 200 °C.
	0.2207 nm (2–10)	0.22062 nm (110)				[16]	Bi_2Te_3 nanosheets were synthesized by dissolving $Bi(NO_3)_3$, TeO_2, and PVP in ethylene glycol, adding KOH, and then microwave-heating the mixture for 15 minutes to produce the final product.
	032 nm (015)	1 nm (003)				[17]	Bi_2Te_3 thin films were produced by electron-beam evaporation of high-purity Bi_2Te_3 onto glass substrates under high vacuum, followed by optional vacuum annealing at 100–300 °C.
	0.322 nm@ (015)	0.238 nm# (1010)		0.322 nm$ (015)	0.322 nm% (015)	[18]	Bi_2Te_3 nanostructures were synthesized by dissolving $BiCl_3$ and Te powder in water, adjusting the solution to pH 14, adding $NaBH_4$ and EDTA-2Na, and then performing a 180 °C hydrothermal treatment for 24 h. @- Bi_2Te_3 synthesized with DMF #- Bi_2Te_3 synthesized with ethylene glycol + EDTA $- Bi_2Te_3 synthesized with deionized water %- Bi_2Te_3 synthesized with deionized water at pH 10
	0.323 nm (0 1 5)	0.225 nm (1 0 10)	0.236 nm (0 1 11)			[19]	Bi_2Te_3 nanorods were compacted into wafers by uniaxial pressing, sealed under Ar and annealed at 500 °C, after which bars were cut and polished for thermoelectric measurements.
	0.320 nm (015)					[20]	Bi–Te and Co-doped Bi_2Te_3 thin films (~300 nm) were deposited at room temperature by DC magnetron sputtering from Bi, Te, and Co targets under Ar at 1×10^{-2} Torr, with composition controlled by the applied powers.
	032 nm (015)					[21]	Bi_2Te_3 was synthesized by dissolving stoichiometric $BiCl_3$ and Te in water, adjusting the pH, adding

							$NaBH_4$ and EDTA-2Na, and then performing a 180 °C hydrothermal reaction for 24 h.
	1.002 nm (003)					[22]	Bi_2Te_3 was synthesized by mixing $BiCl_3$, Na_2TeO_3, NaOH, $NaBH_4$, and an organic additive in water, ultrasonically pre-reacting the mixture, and then hydrothermally treating it at 180 °C for 48 h.
	1.0 nm (003)					[23]	BTA nanorods were synthesized by dissolving $BiCl_3$, NH_4Cl, EDTA, SDBS, and Na_2TeO_3 in water, adding hydrazine, and then performing a 170 °C hydrothermal reaction for 12
	0.238 nm (1010)					[24]	Bi_2Te_3 bulk was produced by cold-pressing stoichiometric Bi and Te powders and then sintering the compact under high-temperature, high-pressure (HPHT) conditions in a cubic press for 30 minutes
	0.219 nm (110)					[25]	Bi_2Te_3 was synthesized via a solvothermal process by mixing Bi_2O_3, TeO_2, and PVP in ethylene glycol, followed by autoclave treatment and subsequent washing and drying.
	0.328 nm (015)	0.381 nm (101)		0.32 nm* (015)	0.378 nm* (101)	[26]	Bi_2Te_3 nanostructures were synthesized hydrothermally at 180 °C for 24 h from $BiCl_3$ and Te precursors in alkaline aqueous solution, with or without surfactants, followed by washing and vacuum drying. *Bi_2Te_3 nanoplates with PVP
	0.324 nm (015)					[27]	Bi_2Te_3 and Ce/I-doped Bi_2Te_3 nanopowders were synthesized by a low-temperature double-solvent sol-gel route in which Bi and dopant ions were dissolved in ethylene glycol, Te and I in acetic acid, the solutions combined, dried, and calcined under argon to obtain nanosized powders.
	0.32 nm (015)					[28]	Te@Bi_2Te_3 core–shell nanorods were synthesized by reducing telluric acid in DEG with hydrazine and PVP at 0 °C to form Te nanorods, followed by addition of triphenylbismuth to form the Bi_2Te_3 shell, and the products were collected by centrifugation and washing
	0.219 nm (110)					[29]	Bi_2Te_3 nanowires were electrodeposited into two-step anodized alumina membranes using a gold-coated AAM as the working electrode and a Bi/$HTeO_2^+$ acidic electrolyte, followed by rinsing and drying for analysis.
	0.322 nm (015)	0.219 nm (110)		0.219 nm (110)		[30]	Bi_2Te_3 nanowires were grown at room temperature inside porous anodic alumina by electrodeposition from an acidic Bi/$HTeO_2^+$ electrolyte, using Au-coated PAA templates and deposition modes optimized by cyclic voltammetry under galvanostatic, potentiostatic, or pulsed conditions
	0.203 nm[&] (0 0 15)	0.507nm* (006)				[31]	Bi_2Te_3 powders were hydrothermally synthesized in a Teflon-lined autoclave at 150–210 °C for 24 h from $BiCl_3$ and Te with NaOH, $NaBH_4$, and Na_2-EDTA, followed by filtration, washing, and vacuum drying. & synthe-sized at 180 °C for 24 h

							*notube synthesized at 210 °C.
	0.137 nm (0 1 20)					[32]	Bi_2Te_3 nanoparticles were prepared by microwave-assisted reduction of Bi^{3+} and Te^{4+} tartarate solutions with hydrazine under alkaline conditions, followed by washing and drying under inert atmosphere.
	0.325 nm (015)	0.231nm 1010)				[33]	Bi_2Te_3 nanowire-array films were deposited by PVD from high-purity Bi_2Te_3 powder onto cleaned glass substrates under high vacuum, with the deposition rate controlled by the evaporation current.
	0.219 nm (110)					[34]	Bi_2Te_3@Sb_2Te_3 core–shell nanocrystals were synthesized via a two-step hydrothermal reduction in ethylene glycol, first forming Bi_2Te_3 nanoplates at 180 °C and then growing the Sb_2Te_3 shell at 190 °C, followed by washing and vacuum drying.
	0.219 nm (110)					[29]	Bi_2Te_3 nanowires were electrodeposited into Au-coated anodic alumina membranes from a $Bi/HTeO_2^+$ electrolyte at 2.5 mA cm^{-2} for 2 h, then rinsed and air-dried for characterization.
	0.314 nm (015)0.229 nm	0.314 nm (015)				[35]	Ag/Bi_2Te_3 segmented nanowires were electrodeposited in AAO templates using a three-electrode cell and alternating pulsed potentials (–0.3 and –1.3 V vs. SCE) in a mixed Ag–Bi–Te electrolyte.
2-Bi50Te-BM1b	0.325 nm (014)	0.236 nm* (110)				a	*tt
	0.229 nm (110)					[36]	BiTe nanobelts were grown by vapor transport in a two-zone furnace by evaporating Bi_2Te_3 powder at ~500 °C under controlled Ar flow and low pressure, allowing the vapor to deposit onto Si substrates downstream.
Bi_4Te_3	0.310 nm (107)					[37]	Bi_4Te_3 was obtained by heating $(Et_2Bi)_2Te$ (0.3 mmol) in DIPB at 80 °C for 14 h under argon, followed by precipitation with methanol and purification by centrifugation and chloroform washing.
5-Bi70Te-BM1	0.322 nm (013)	0.321 nm* (013)				a	*tt

Supplementary Note 3: Thermal analysis

The new refined version of the Bi-Te phase diagram [57] shows the compounds Bi_2Te_3, Bi_4Te_5, Bi_8Te_9, BiTe, Bi_4Te_3, Bi_2Te, and Bi_7Te_3 with practically constant compositions and revealed that all of these compounds, except for Bi_2Te_3, melt with decomposition by peritectic reactions. It was found that Bi_2Te_3 melts congruently at 586°C, and the rest melt with peritectic reactions at 562°C (Bi_4Te_5), 550°C (Bi_8Te_9), 542°C (BiTe), 435°C (Bi_4Te_3), 392°C (Bi_2Te), and 332°C (Bi_7Te_3).

Table S 6. List of phase transition temperatures for the Bi-Te system.

Sample ID	Decomposition Temperature in air	Decomposition Temperature in Argon
1-Bi50Te-BM1a	melted @ 574°C	Bi-Te-O formation > 400°C stable above 650°C
2-Bi50Te-BM1b	Transition to Bi_2TeO_7 @ 500°C	Decomposed > 520°C
5-Bi70Te-BM1	Decomposed to Bi >500°C	Decomposed >300°C

Supplementary Note 4: SEM-EDS data

Particle size distributions derived from SEM images in Figure S14 exhibit similar trends but are shifted toward larger apparent sizes. This is attributed to particle agglomeration at the submicron scale. In turn, SEM micrographs reveal submicron-sized agglomerates with lamellar or plate-like morphologies. This contrast between nanoscale features (TEM) and microscale aggregates (SEM) highlights the hierarchical structure induced by mechanical milling and reinforces the distinction between particle size (TEM) and crystallite size (XRPD).

EDS analysis confirms that the nominal Bi:Te ratio is retained, despite significant oxygen incorporation from the precursors. The C peak was labeled, and its origin is commonly related to the high background counts in SEM-EDS, which create an artificial carbon peak. This artifact is due to the window in the detector, which has a specific transmission profile with a strong absorption edge just above but very close to the carbon X-ray energy.

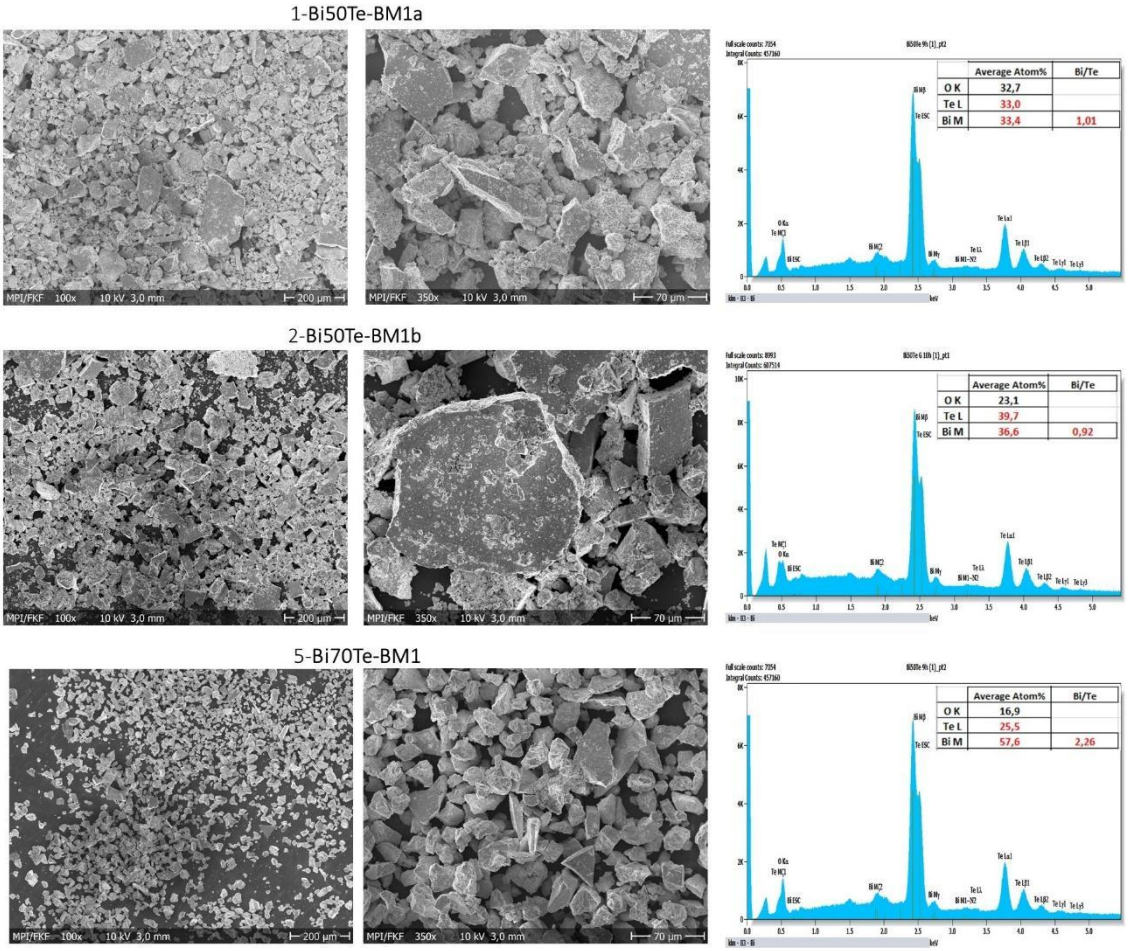

Figure S 14. SEM images, EDS spectra and average chemical analysis for main samples.

Supplementary Note 5: XRD analysis of the sintered pallets

The profile fitting of the Bi-Te samples is shown in Figure S 15 measured after the thermoelectric (TE) characterization. These samples were sintered at 300°C for 1h, which improved crystallization as seen by the narrow peaks in the pattern. Fitting required the use of BiTe Tsumoite phases (space group 164, PDF#00-031-0200) for $Bi_{50}Te_{50}$ samples and Bi_2Te phases (space group 164, PDF#04-019-6786) for the $Bi_{70}Te_{30}$ samples. Excess of Bi was found for the $Bi_{70}Te_{30}$ phases (see Figure S 15(c,d)). Modelling the pattern with the conventional whole powder pattern analysis using the Rietveld approach provided non-satisfactory adjustments. Bi-Te phases are known for having many stacking fault mechanisms that cannot be modelled and escape the scope of this paper. However, one way of qualitatively understanding the presence of the stacking faults and other defects in the sample is by analyzing the agreement factors. If higher, they mean that the presence of stacking faults is increased since it does not conform to the unfaulted BiTe model. For a meaningful analysis, the measurements were taken in the very same condition and modelled with the same parameters. The analysis reveals that the $Bi_{50}Te_{50}$-BM1 has an Rwp of 6.95% while $Bi_{50}Te_{50}$-BM2 samples have an Rwp of 14.77 %. $Bi_{70}Te_{30}$-BM1

sample has an Rwp of 6.73% while $Bi_{70}Te_{30}$-BM2 sample has an Rwp of 8.03%. Therefore, samples with BM1 qualitatively present lower stacking faults and other defects after the TE measurements. Another aspect observed is the crystallinity of the BM1 samples, notably higher than the BM2 samples since the relative intensity is also higher (graphs are plotted on the same scale). This happens despite the use of a higher ball-to-powder ratio (BPR) and milling times for BM1. This points out the effect of the reagents used that are playing a role in crystallization and reduction of faults.

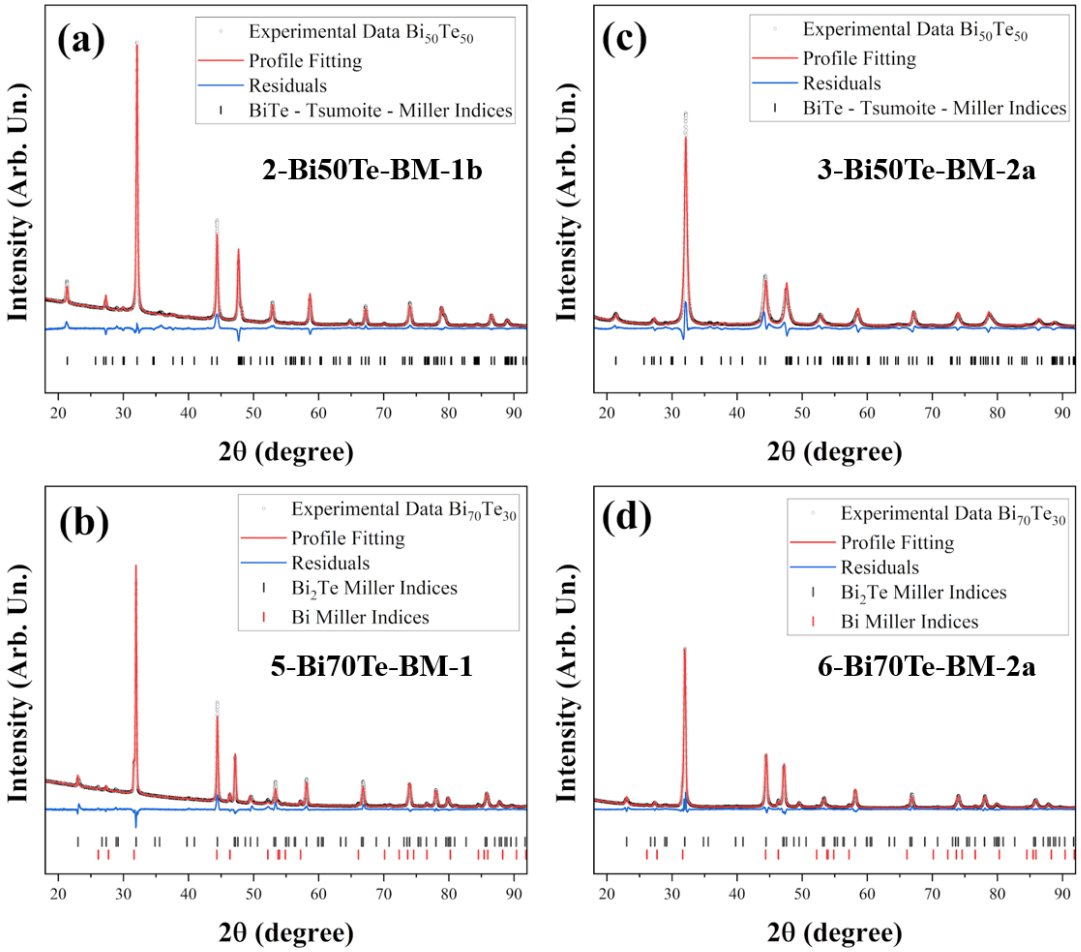

Figure S 15. XRD powder pattern modelling of the pallets used for thermoelectric characterization. (a) 2-Bi50Te50-BM1b, (b) 3-Bi50Te50-BM2a, (c) 5-Bi70Te30-BM1, and (d) 6-Bi70Te30-BM2a, Circular markers represent experimental data, red lines the profile fitting, and blue lines the residuals; vertical ticks indicate Bragg reflection positions of the identified phases.

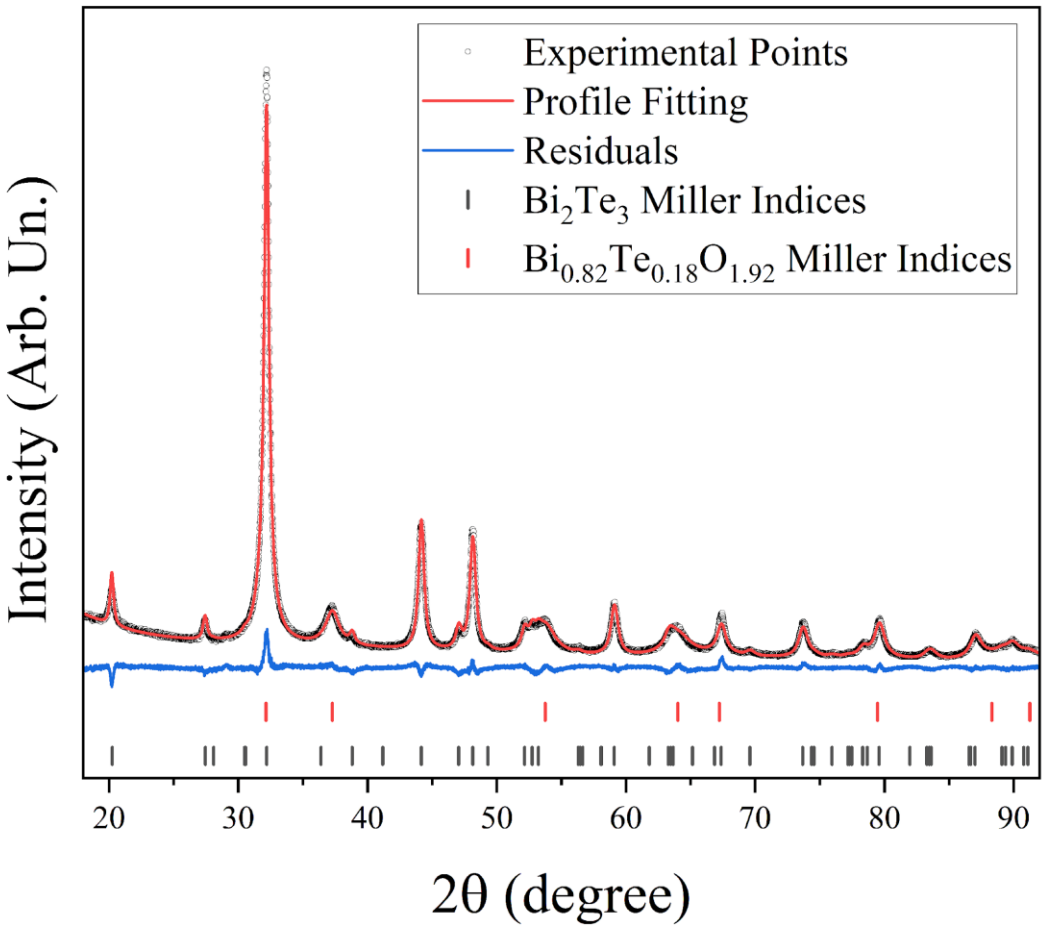

Figure S 16. XRD pattern fitting of the 1-Bi50Te-BM1a pallet used for thermoelectric characterization. Circular markers represent the experimental data collected using Co-K_α radiation, red lines the profile fitting, and blue lines the residuals. The Miller indices are represented by tick markers: black for Bi_2Te_3 and red for the $Bi_{0.82}Te_{0.18}O_{1.92}$ phases.

Supplementary Note 6: Additional Thermoelectric characterization and reproducibility

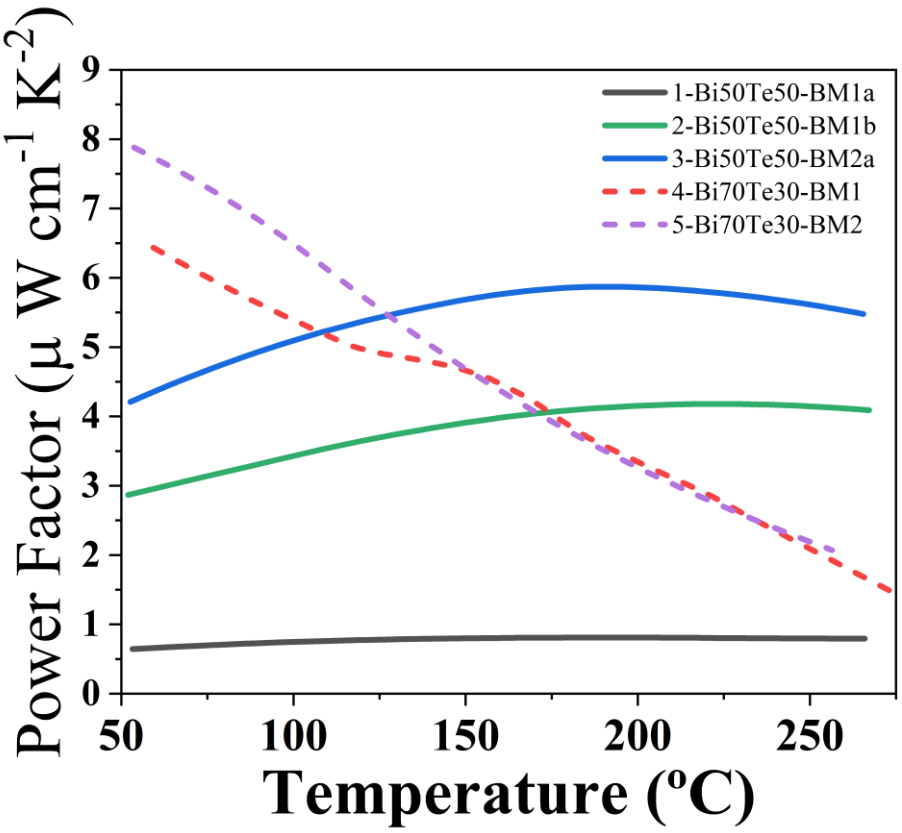

Figure S 17. Power factor estimated from the Seebeck and resistivity values of figure 7 in the main text.

The plots show that the samples have small hysteresis in the Seebeck values, however, it is very reproducible. This hysteresis is characteristic of heating and cooling ramps, since the thermal kinetics differ. No visible sample morphology, colour was observed after the measurements. Thermal diffusivity cycles are not shown, since they are not so sensible to any hysteresis present during the measurements compared to the electronic properties.

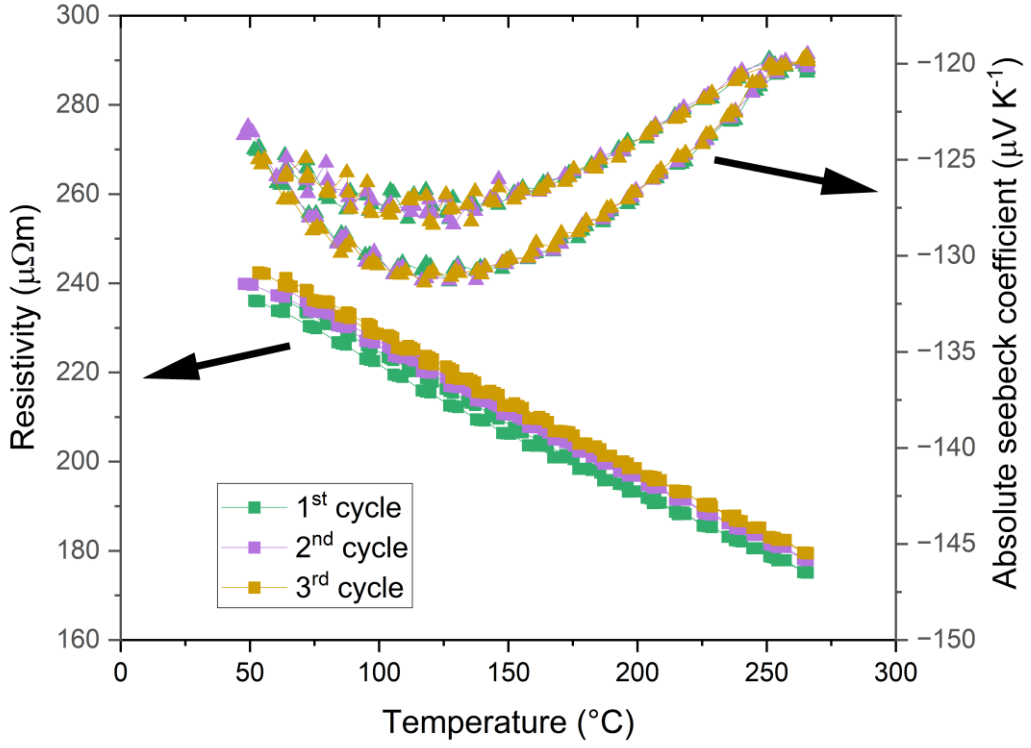

Figure S 18. Electronic properties for the 1-Bi50Te-BM1a samples. Resistivity (on the left, given by the squares) and Seebeck coefficients (on the right, given by the triangles) for three measurement cycles.

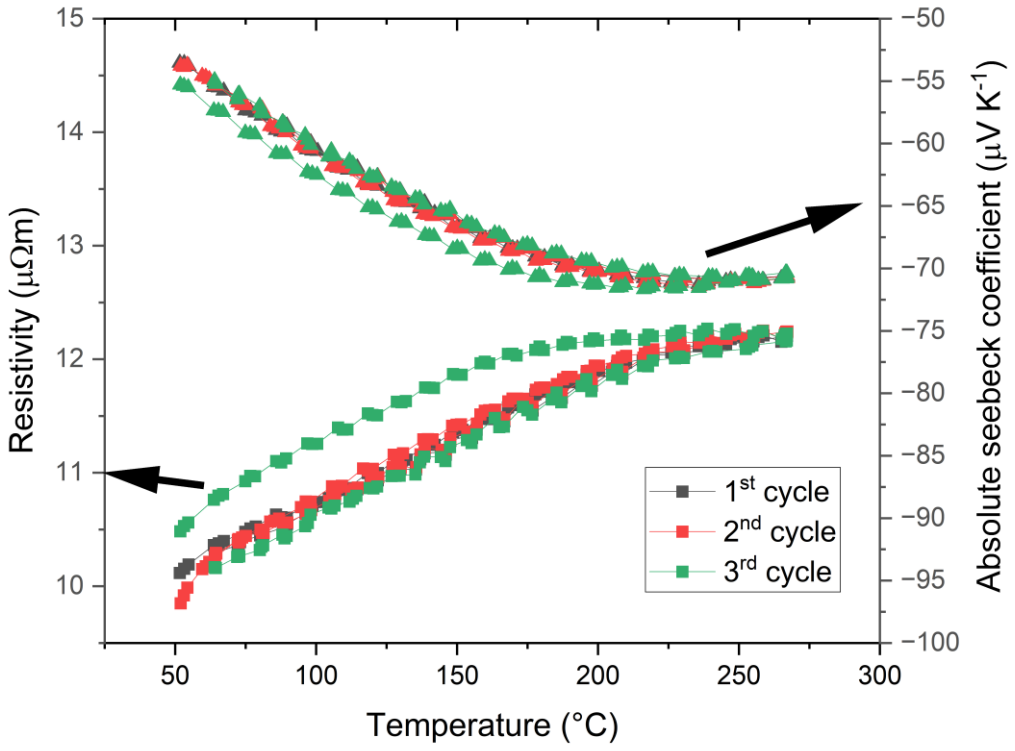

Figure S 19. Electronic properties for the 2-Bi50Te-BM1b samples. Resistivity (on the left, given by the squares) and Seebeck coefficients (on the right, given by the triangles) for three measurement cycles.

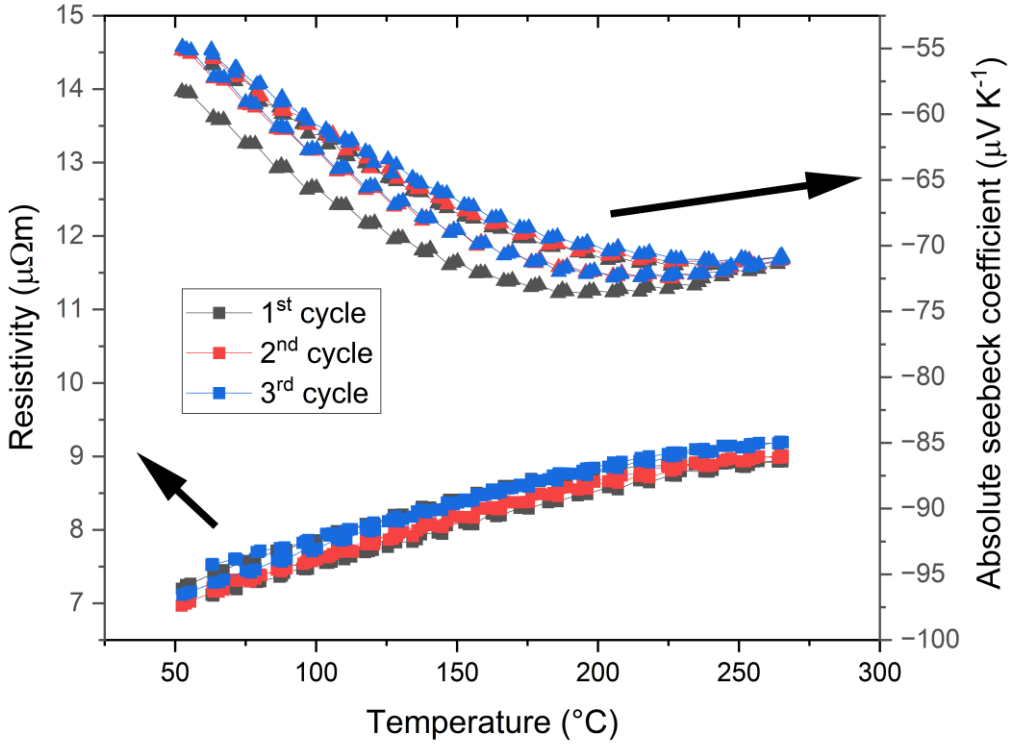

Figure S 20. Electronic properties for the 3-Bi50Te-BM2a samples. Resistivity (on the left, given by the squares) and Seebeck coefficients (on the right, given by the triangles) for three measurement cycles.

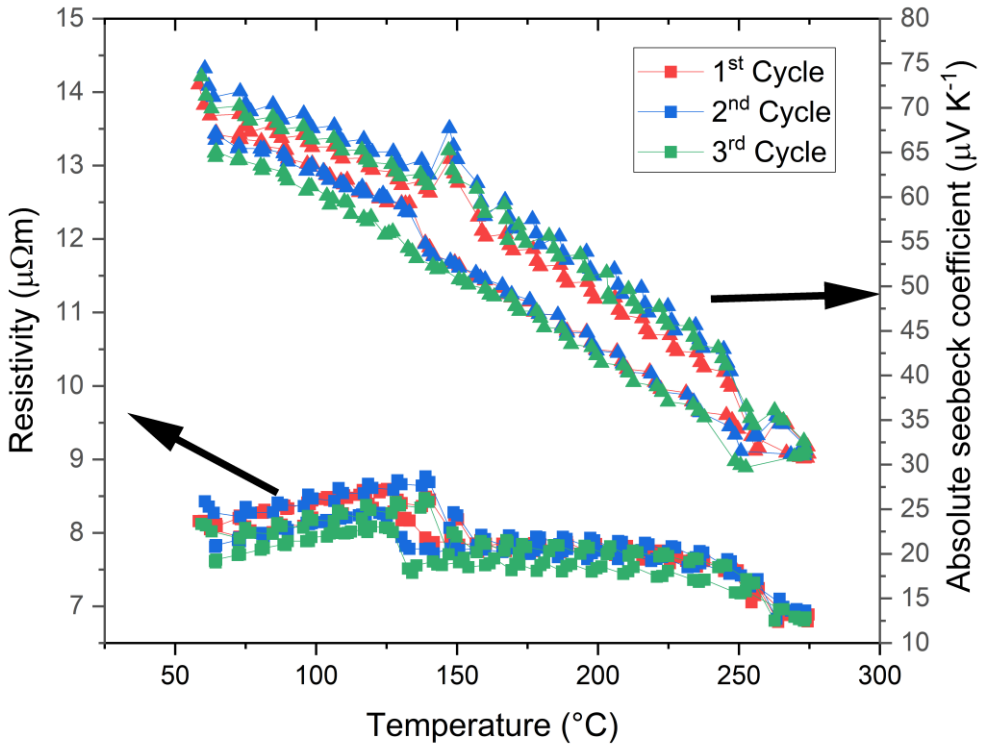

Figure S 21. Electronic properties for the 5-Bi70Te-BM1 samples. Resistivity (on the left, given by the squares) and Seebeck coefficients (on the right, given by the triangles) for three measurement cycles.

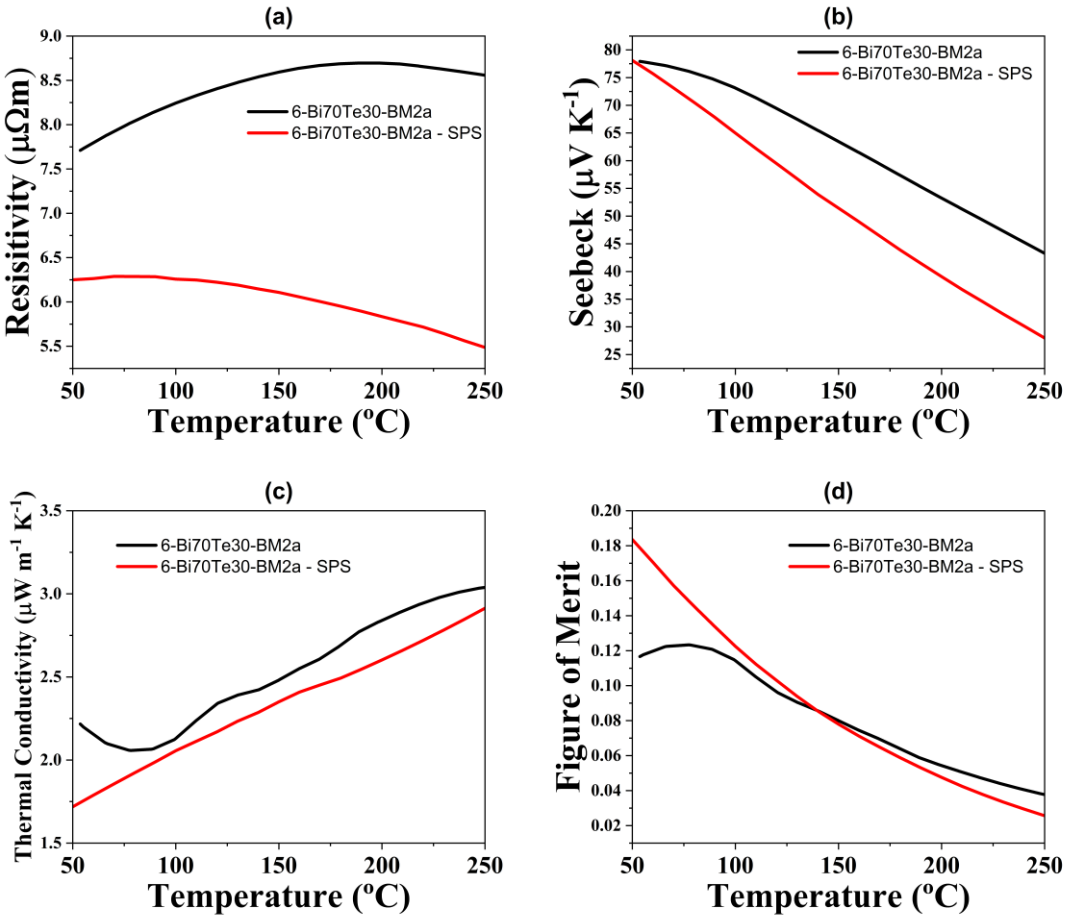

Figure S 22. Comparison of the thermoelectric properties of cold-pressed and SPS samples of 6-Bi70Te-BM2a. (a) Resistivity, (b) Seebeck coefficient, (c) thermal conductivity, (d) figure of merit. Black lines represent the low density cold-pressed sample values, and red the SPS sample values.

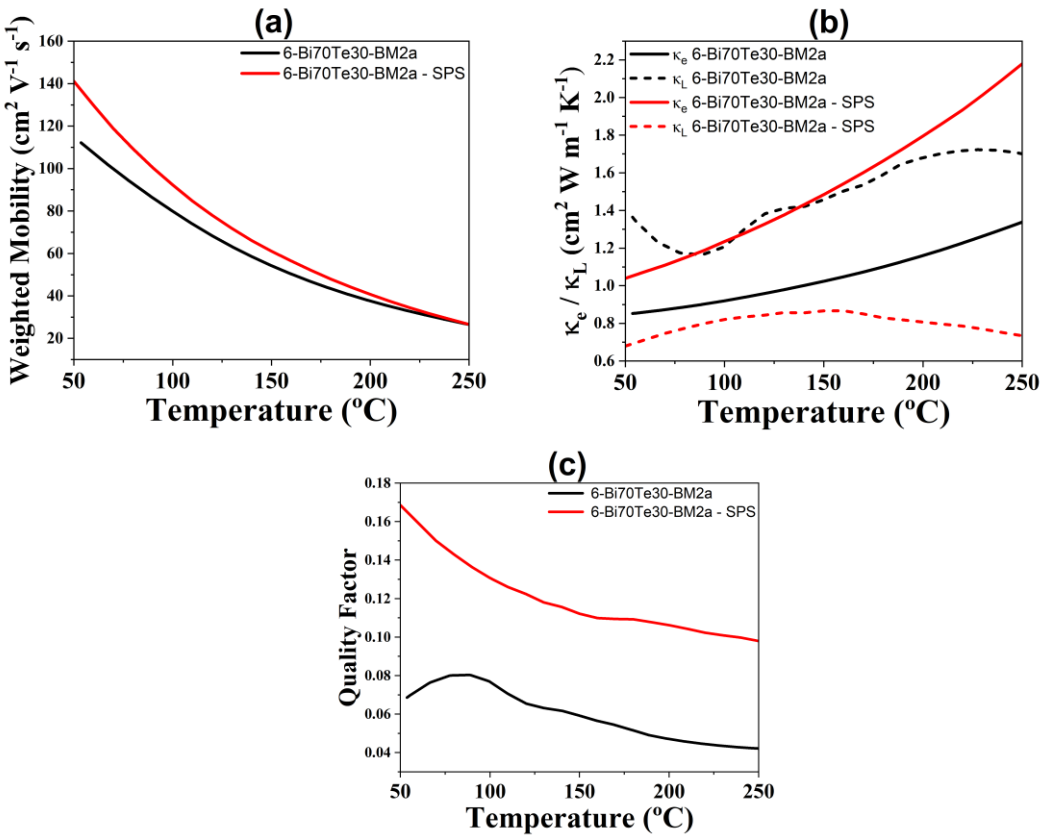

Figure S 23. Comparison of the thermoelectric properties of cold-pressed and SPS samples of 6-Bi70Te-BM2a. (a) weighted mobility, (b) lattice (κ_L- dashed lines) and electronic (κ_e - solid lines) thermal conductivities, and (c) quality factor. Black lines represent the low density cold-pressed sample values, and red the SPS sample values.

Supplementary Note 7: calculation of lattice thermal conductivity, quality factor and weighted mobility

To estimate the total thermal conductivity (κ) is given by the following:

$$\kappa = D\ \rho\ C_p \qquad \text{(equation S 1)}$$

Where D is the thermal diffusivity, ρ is the geometrical density and C_p is the heat capacity given in Table S 2. ρ was estimated by measuring the mass and the dimensions of the pallet. C_p values were obtained using the Kopp–Neumann law relationship:

$$C_p = \sum_i w_i\ M_i\ C_{p_i} / \sum_i w_i\ M_i \qquad \text{(equation S 2)}$$

Where the atomic fraction is represented by w_i and M_i is the molar mass of the atom i. The sum covers all atom types in the phase. C_{p_i} values are given by the Duolong-Petit approximation:

$$C_{p_i} = \frac{3\ R}{M_i} \qquad \text{(equation S 3)}$$

The lattice thermal conductivity, κ_L, was estimated by subtracting the electronic contribution (κ_e)to the total thermal conductivity (κ):

$$\kappa_L = \kappa - \kappa_{el} \qquad \text{(equation S 4)}$$

Where κ_e was estimated via the Wiedemann–Franz law:

$$\kappa_{el} = L\,\sigma\,T \qquad \text{(equation S 5)}$$

With L being the Lorenz number, σ the electronic conductivity, and T the absolute temperature. L is estimated via the following relationship [38]:

$$\frac{L}{10^{-8}\ W\Omega\mathrm{K}^{-2}} = 1.5 + \exp\left(\frac{|S|}{116\ \mu V\ K^{-1}}\right) \qquad \text{(equation S 6)}$$

In the single parabolic band (SPB) model, the quality factor B is given by:

$$B\ = \left(\frac{k_B}{e}\right)^2\ \ \frac{8\,\pi\,e\,(2\,m_e\,k_B\,T)^{\frac{3}{2}}}{3\,h^3}\ \left(\frac{\mu_w}{\kappa_L}T\right) \qquad \text{(equation S 7)}$$

where $k_B$and h are the Boltzmann and Planck constants, respectively [63].

The weighted mobility (μ_W) can be estimated empirically from the measured S and ρ values given the relationship of Snyder et. al [16] :

$$\mu_W = 331\frac{cm^2}{V\,s}\left(\frac{m\,\Omega\,cm}{\rho}\right)\left(\frac{T}{300\ K}\right)^{-\frac{3}{2}}\left[\frac{\exp\left[\frac{|S|}{k_B/e}-2\right]}{1+\exp\left[-5\left(\frac{|S|}{k_B/e}-1\right)\right]}+\frac{\frac{3}{\pi^2}\frac{|S|}{k_B/e}}{1+\exp\left[5\left(\frac{|S|}{k_B/e}-1\right)\right]}\right] \qquad \text{(equation S 8)}$$

Weighted mobility combines the effects of carrier mobility and density-of-states effective mass (m^*),

$$\mu_w = \mu\left(\frac{m^*}{m_e}\right)^{3/2} \qquad \text{(equation S 9)}$$

making it a strong indicator of intrinsic electronic quality.

References

[1] H. Xu *et al.*, “Vibrational properties of epitaxial Bi4Te3 films as studied by Raman spectroscopy,” no. April 2022, pp. 0–7, 2024.

[2] “Vibrational spectra of bismuth oxide and the sillenite-structure bismuth oxide derivatives *,” vol. 34, 1977.

[3] A. C. Gandhi, C.-L. Cheng, and S. Y. Wu, “Structural and Enhanced Optical Properties of Stabilized γ–Bi2O3 Nanoparticles Effect of Oxygen Ion Vacancies.pdf,” *Nanomaterials*, vol. 10, p. 1023, 2020.

[4] C. Matter, “Raman spectra in as a function of the temperature and the polarization and the polarization,” *J. Phys. Condens. Matter*, vol. 10, no. 3659, 1998.

[5] V. N. Moiseyenko, N. P. Brynza, B. A. Sal, R. Holze, and V. S. Gorelik, “Raman Scattering in Nanocomposites Based on Synthetic Opal,” vol. 54, no. 12, pp. 1250–1255, 2018.

[6] V. Russo *et al.*, “Raman spectroscopy of Bi-Te thin films,” no. January, pp. 205–210, 2008.

[7] P. I. Kuznetsov *et al.*, “Growth of Bi 2 Te 3 fi lms and other phases of Bi-Te system by MOVPE,” *J. Cryst. Growth*, vol. 455, no. September, pp. 122–128, 2016.

[8] M. Galva *et al.*, “Controlling the Epitaxial Growth of Bi 2 Te 3 , BiTe , and Bi 4 Te 3 Pure Phases by Physical Vapor Transport,” 2018.

[9] O. Caballero-Calero, C. V. Manzano, A. Cantarero, and M. Martín-González, “Geometry-driven plasmonic heating in Bi_2Te_3 nanostructures Intrinsic surface plasmons enable enhanced thermoelectric voltage.pdf,” *Chem. Eng. J.*, vol. 523, no. 168220 Contents, 2025.

[10] X. Qi, W. Ma, X. Zhang, and C. Zhang, “Applied Surface Science Raman characterization and transport properties of morphology-dependent two-dimensional Bi 2 Te 3 nano fi lms,” *Appl. Surf. Sci.*, vol. 457, no. May, pp. 41–48, 2018.

[11] K. M. F. Shahil;, M. Z. Hossain;, V. Goyal;, and A. A. Balandin, “Micro-Raman spectroscopy of mechanically exfoliated few- quintuple layers of Bi2 Te3, Bi2Se3, and Sb2Te3 materials ?,” vol. 054305, no. April 2010, 2014.

[12] O. Caha *et al.*, “Growth, Structure, and Electronic Properties of Epitaxial Bismuth Telluride Topological Insulator Films on BaF 2 (111) Substrates,” vol. 2, no. 111, 2013.

[13] P. Sujita, S. Vadivel, G. N. Banu, and B. Neppolian, “Layered -bismuthene maximizes the active sites in Bi 2 Te 3 towards electrocatalytic hydrogen evolution reactions,” *J. Alloys Compd.*, vol. 1003, no. April, p. 175483, 2024.

[14] Y. Xu, Z. Ren, G. Cao, W. Ren, K. Deng, and Y. Zhong, “Synthesis of single crystal Bi 2 Te 3 nanoplates via an inorganic-surfactant-assisted solvothermal route,” vol. 62, pp. 4525–4528, 2008.

[15] J. Kim *et al.*, “Hydrothermal synthesis of Bi 2 Te 3 nanowires through the solid-state interdiffusion of Bi and Te atoms on the surface of Te nanowires,” *J. Cryst. Growth*, vol. 312, no. 22, pp. 3410–3415, 2010.

[16] Z. Li, R. Teng, S. Zheng, Y. Zhang, T. Huang, and G. Lu, “Single-crystalline Bi 2 Te 3 nanosheets with uniform morphology via a simple , ef fi cient , and high-yield microwave-assisted synthesis,” *J. Cryst. Growth*, vol. 406, pp. 104–110, 2014.

[17] C. Sudarshan, S. Jayakumar, K. Vaideki, and C. Sudakar, “Effect of vacuum annealing on structural , electrical and thermal properties of e-beam evaporated Bi 2 Te 3 thin fi lms,” *Thin Solid Films*, vol. 629, pp. 28–38, 2017.

[18] P. Shyni and P. P. Pradyumnan, “Physica E : Low-dimensional Systems and Nanostructures Effect of polar solvents on the growth , morphology and thermoelectric properties of Bi 2 Te 3 nano particles,” *Phys. E Low-dimensional Syst. Nanostructures*, vol. 138, no. April 2021, p. 115072, 2022.

[19] G. Yuan, Y. Li, N. Bao, J. Miao, C. Ge, and Y. Wang, “Facile synthesis and thermoelectric studies of n-type bismuth telluride nanorods with cathodic stripping Te electrode,” *Mater. Chem. Phys.*, vol. 143, no. 2, pp. 587–594, 2014.

[20] M.-C. Chuang, S.-C. Chen, C.-L. Chen, W.-Y. Chen, S.-W. Chou, and H. Sun, “Cobalt atom incorporation regulates grain structure and thermoelectric properties in Bi_2Te_3 thin films,” *Surf. Coatings Technol.*, vol. 516, no. 132714, 2025.

[21] P. Shyni and P. P. Pradyumnan, “Materials Science & Engineering B Deep tuning of Bi 2 Te 3 nanostructures suitable for thermoelectric waste heat recovery : The impact of pH on crystal growth in hydrothermal synthesis,” *Mater. Sci. Eng. B*, vol. 287, no. October 2022, p. 116090, 2023.

[22] Z. Wang, F. Wang, H. Chen, L. Zhu, H. Yu, and X. Jian, “Synthesis and characterization of Bi 2 Te 3 nanotubes by a hydrothermal method,” vol. 492, pp. 50–53, 2010.

[23] C. Yu *et al.*, “Preparation and thermoelectric properties of inhomogeneous bismuth telluride alloyed nanorods,” *J. Alloys Compd.*, vol. 570, pp. 86–93, 2013.

[24] Y. Zhang *et al.*, “Evolution of thermoelectric properties and anisotropic features of Bi 2 Te 3 prepared by high pressure and high temperature,” *J. Alloys Compd.*, vol. 632, pp. 514–519, 2015.

[25] S. Vinoth, T. Balaganapathi, B. Kaniamuthan, T. Arun, and I. P. Muthuselvam, “Bi 2 Te 3 thin hexagonal nanoplatelets : Synthesis and its characterization studies,” *Phys. E Low-dimensional Syst. Nanostructures*, vol. 92, no. April, pp. 17–22, 2017.

[26] P. Shyni and P. P. Pradyumnan, “Materials Today : Proceedings Bi 2 Te 3 nanotubes and nanoplates for thermoelectric applications : Effect of surfactant on crystal growth,” *Mater. Today Proc.*, vol. 65, pp. 293–297, 2022.

[27] S. Irfan, J. Luo, F. Ping, and Z. Zhuanghao, “Theoretical and experimental investigation of magnetic properties of iodine and cerium Co-doped Bi 2 Te 3 nanoparticles,” *Integr. Med. Res.*, vol. 9, no. 6, pp. 13893–13901, 2020.

[28] H. Dong, R. Popescu, D. Gerthsen, and C. Feldmann, “Shape-stabilized Bi 2 Te 3 -capped Tellurium Nanorods,” no. 14, pp. 2406–2410, 2013.

[29] C. Jin, X. Xiang, C. Jia, W. Liu, W. Cai, and L. Yao, “Electrochemical Fabrication of Large-Area , Ordered Bi 2 Te 3 Nanowire Arrays,” pp. 1844–1847, 2010.

[30] J. Lee, S. Farhangfar, J. Lee, L. Cagnon, R. Scholz, and G. Ulrich, “Tuning the crystallinity of thermoelectric Bi 2 Te 3 nanowire arrays grown by pulsed electrodeposition,” 2008.

[31] H. J. Kim, M. Han, H. Kim, W. Lee, and S. Kim, “Morphology Controlled Synthesis of Nanostructured Bi 2 Te 3,” vol. 33, no. 12, pp. 3977–3980, 2012.

[32] S. Pradhan, R. Das, R. Bhar, R. Bandyopadhyay, and P. Pramanik, “A simple fast microwave-assisted synthesis of thermoelectric bismuth telluride nanoparticles from homogeneous,” 2017.

[33] Y. Deng, Y. Xiang, and Y. Song, “Template-free Synthesis and Transport Properties of Bi 2 Te 3 Ordered Nanowire Arrays via a Physical Vapor Process & DESIGN 2009,” pp. 5–8, 2009.

[34] L. L. Yuan and D. Yao, “Epitaxial formation of core – shell heterostructured,” 2014.

[35] J. Fu *et al.*, “Large-scale synthesis and characterisation of Ag / Bi 2 Te 3 superlattice nanowires via pulse electrodeposition,” vol. 8, pp. 188–190, 2013.

[36] K. Pillai, “Synthesis of single crystalline BiTe nanobelts by catalyst-free vapor transport method Synthesis of single crystalline BiTe nanobelts by catalyst-free vapor transport

method."

[37] G. Bendt, A. Weber, S. Heimann, W. Assenmacher, O. Prymak, and S. Schulz, "Wet-chemical synthesis of different bismuth telluride nanoparticles using metal organic precursors – single source vs. dual source approach," pp. 14272–14280, 2015.

[38] H. Kim, Z. M. Gibbs, Y. Tang, H. Wang, and G. J. Snyder, "Characterization of Lorenz number with Seebeck coefficient measurement," no. September, 2020.